ISSN 0915-633X

NATIONAL INSTITUTE FOR FUSION SCIENCE

Roles of Bumpy Field on Collisionless Particle Confinement in Helical-Axis Heliotrons

M. Yokoyama, N. Nakajima, M. Okamoto,
Y. Nakamura and M. Wakatani

(Received - Jan. 29, 1999)

NIFS-583 Feb. 1999

RESEARCH REPORT
NIFS Series

NAGOYA, JAPAN

Roles of Bumpy Field on Collisionless Particle Confinement in Helical-Axis Heliotrons

M.Yokoyama, N.Nakajima, M.Okamoto

National Institute for Fusion Science, Toki 509-5292, Japan

Y.Nakamura, M.Wakatani

Graduate School of Energy Science, Kyoto University, Uji, 611, Japan

Abstract

Roles of bumpy field on collisionless particle confinement in helical-axis heliotrons are investigated with the model magnetic field and particle orbit calculations in the Boozer coordinates. The mod-B_{min} contours can be shifted in the major radius direction with the control of the bumpy field, where B_{min} is the minimum value of $|B|$ in the toroidal direction within one field period. The area of closed mod-B_{min} contours is a useful measure to evaluate global collisionless particle confinement as long as the mod-B_{min} contours connect toroidally. Negative value of ratio between the bumpy and the helicity components contributes to obtain the largest area of closed mod-B_{min} contours for finite ratio between the toroidicity and the helicity components. The radial variation of the bumpy field attributes to realize a toroidally localized mod-B_{min} structure, which is significantly effective to improve collisionless particle confinement.

Keywords

bumpy field, collisionless particle, mod-B_{min} contour, helical-axis heliotron

1 Introduction

A new concept, helical-axis heliotron [1], has been proposed for constructing the new experimental device (Heliotron J [2]) after Heliotron E [3] at the Institute of Advanced Energy (IAE), Kyoto University. The study of heliotron configurations originally developed at Kyoto University continues in Japan and led to realize the optimized heliotron device, the Large Helical Device (LHD) [4] at the National Institute for Fusion Science (NIFS).

The compatibility between good particle confinement and sufficient magnetohydrodynamic (MHD) stability has been pursued in the Heliotron E (major radius $R_0 = 2.2$ m, minor radius $a = 0.2$ m and magnetic field strength $B = 2$ T), however; it has been rather difficult. The particle confinement can be improved both in ECH and NBI plasmas for the magnetic configuration with the magnetic axis shifted 2 cm inward at zero beta. However, this magnetic configuration has a rather high magnetic hill and clear MHD instabilities are typically observed [5]. On the other hand, configurations with the magnetic axis shifted outward to enhance magnetic well deteriorate particle confinement particularly in finite beta plasmas. The one way to break this incompatibility was the application of toroidal field of about 5 % of main helical field to form shallow magnetic well in the plasma core region, which improves the MHD stability up to $\langle\beta\rangle \sim 1\%$ [6]. Here $\langle\beta\rangle$ denotes the volume averaged beta value. To pursue further improvement or compatibility between good particle confinement and sufficient MHD stability to surpass these experimental results, it is necessary to form vacuum magnetic well in the entire plasma region, especially in the edge region. However, it has not been easy to realize such magnetic configurations in $L = 2$ planar-axis heliotrons, where L is the pole number of the helical coil winding.

The helical-axis heliotron concept arises to release the limitation of planar-axis configurations to realize good particle confinement and sufficient MHD stability simultaneously. The main requirements for this compatibility are the formation of vacuum magnetic well in the entire plasma region and the reduction of ripple transport due to the control of magnetic field ripple. The bootstrap current control is also considered to investigate its effects on plasma confinement properties. The helical-axis heliotron configurations can be produced by the modulated $L = 1$ helical coil as shown in Ref. [1]. The coil system is rather simple compared to the modular coil system. Therefore, there is a sufficient space with easy access to the plasma for the heating and diagnostics, and this seems an advantage to design a flexible experimental device.

The main characteristics of helical-axis heliotrons are briefly summarized as follows.

- For the magnetic spectrum in the Boozer coordinates (Boozer spectrum), the bumpy field is comparable to the main helical field with the opposite sign each other, which is effective to suppress neoclassical ripple transport.

- The collisionless particle confinement is improved to some extent in finite beta equilibria.

- The radial electric field can significantly improve collisionless particle confinement even if it is rather small compared to the particle energy.

- The vacuum magnetic well is formed in the entire plasma region to stabilize interchange modes and to investigate effects of magnetic well on those instabilities.

- The magnetic configuration can be controlled relatively in a wide range by changing current ratios in helical, poloidal and toroidal coil sets. Especially, the bumpy field can change its sign by controlling currents in the toroidal coils, and its role on confinement properties can be investigated in a wide range.

- The bootstrap current can also be controlled with the bumpy field.

- There exists a possibility of the natural divertor.

There are some problems to be solved to make the helical-axis heliotron concept more attractive. The Pfirsch-Schlüter current is rather large in the previous study of helical-axis heliotrons [1], which causes a significant change of rotational transform in finite beta equilibria. This may cause the appearance of low order rational surfaces to deteriorate MHD stability, and therefore, the behavior of magnetic islands should also be clarified, for example, by the HINT code [7].

To realize high beta plasma confinement in helical-axis heliotrons, it is also essential to improve particle confinement properties. Since the bumpy field has been negligibly small in conventional planar-axis heliotrons, the typical model magnetic field includes only the torodicity and helicity components other than the uniform magnetic field [8]. However, since the bumpy field typically appears in helical-axis heliotrons, it is essential to understand its roles on plasma confinement properties. As the first step, roles of

bumpy field on collisionless particle confinement will be investigated in this paper.

Generally, helical axis configurations (such as the W7-X [9] and heliacs) have several magnetic field components other than the toroidicity and helicity in the Boozer spectrum [10]. Therefore, it is necessary to examine particle confinement properties not based on the simple model magnetic field, but by following many particle orbits in the realistic configuration to evaluate collisionless particle confinement properties. However, it would be effective to have some guidance for obtaining more attractive physical properties based on a simpler analysis. The typical helical-axis heliotron configuration have predominant helicity, toroidicity and bumpy field component and other components have relatively small amplitude in the Boozer spectrum. Thus, the model magnetic field including the bumpy field is used to grasp effects of the magnetic spectrum on collisionless particle confinement properties in helical-axis heliotrons.

This paper is organized as follows. Section 2 describes characteristics of mod-B_{min} contours in helical-axis heliotrons for clarifying roles of radially constant bumpy field. The appropriate bumpy field to maximize the closed mod-B_{min} area is shown and relationship between the closed mod-B_{min} area and the collisionless particle confinement is examined. It is shown that the toroidal localization of mod-B_{min} contours by the radially varying bumpy field has favorable effects on global collisionless particle confinement in Section 3. Finally, summary will be given in Section 4.

2 Control of Mod-B_{min} Structure with the Bumpy Field

To study particle confinement properties in realistic magnetic configurations, it usually require time consuming orbit following calculations. However, if one considers only deeply trapped particles, it is possible to predict their trajectories only by the structure of the magnetic field strength. The reason can be explained by using the longitudinal adiabatic invariant J, which can be expressed as $J = m \oint v_{||} dl$ $\propto \sqrt{E - \mu B_{min} - e\Phi}$ also in helical systems. Here (E, μ, e) is (kinetic energy, magnetic moment, charge) of the particle, Φ the electric field potential and B_{min} the smallest magnetic field strength along the magnetic field line in one helical pitch. Since particles move with keeping E and μ, the deeply trapped particles can be considered to follow the line of $B_{min} + e\Phi/\mu = const.$ When the electric potential is not taken into account, $B_{min} = const$ line corresponds to the deeply trapped particle trajectory. Moreover, in the case of small rotational transform per a field period, $\iota/M \ll 1$, the magnetic field line can be considered to stay in the constant (ψ, θ), and thus, $B_{min} = min_{\zeta}|B(\psi, \theta, \zeta)|$. Here, M is the number of the field period. For analyzing magnetic spectrum, the Boozer coordinates $(\psi, \theta_B, \zeta_B)$ [11] is utilized in this paper, where ψ is the normalized toroidal flux function and θ_B (ζ_B) the poloidal (toroidal) angle.

As the first step to study collisionless particle confinement in helical-axis heliotrons, the mod-B_{min} structure is considered. Since the bumpy field has been negligibly small in conventional heliotrons, the frequently used model magnetic field

has been

$$B/B_0 = 1 - \epsilon_t \cos\theta_B - \epsilon_h \cos(L\theta_B - M\zeta_B)\,, \quad (1)$$

where ϵ_t (ϵ_h) denotes the toroidicity (helicity) of the magnetic field. It is typical that ϵ_h is proportional to $(r/a)^2$ in $L = 2$ planar-axis heliotrons, where r/a is the normalized average radius. On the other hand, since the bumpy field typically appears in helical-axis heliotrons, the above model magnetic field is extended to include it based on the multiple helicity approach [12] as

$$B/B_0 = 1 - \epsilon_T - \epsilon_H \cos(\eta + \alpha)\,, \quad (2)$$

where $\epsilon_T = \epsilon_t \cos\theta_B$, $\epsilon_H = \sqrt{\epsilon_h^2 + 2\epsilon_h\epsilon_b \cos\theta_B + \epsilon_b^2}$ and $\eta = L\theta_B - M\zeta_B$. The phase angle α is defined by $\cos\alpha = (\epsilon_h + \epsilon_b\cos\theta_B)/\epsilon_H$. The ϵ_b denotes the bumpy field component. Both ϵ_t and ϵ_h are assumed to be proportional to (r/a) as typically valid in helical axis heliotrons/stellarators [1, 9, 10]. For convenience, ϵ_t is written as $\epsilon_t = \epsilon_{ta}(r/a)$ and ϵ_h as $\epsilon_h = \epsilon_{ha}(r/a)$, where ϵ_{ta} (ϵ_{ha}) is the toroidicity (helicity) at the plasma edge, respectively. It is also assumed that ϵ_{ha} and ϵ_{ta} are positive as in Ref. [1] by the definition of the model magnetic field, eq.(2). In this section, the bumpy field is assumed to be radially constant for simplicity. The roles of radial variation of the bumpy field will be discussed in Section 3.

It is noted that

$$\frac{B_{min}(x,y)}{B_0} = 1 - \epsilon_{ta}\frac{x}{a} - \sqrt{\epsilon_{ha}^2\frac{x^2+y^2}{a^2} + 2\epsilon_{ha}\epsilon_b\frac{x}{a} + \epsilon_b^2} \quad (3)$$

for the model magnetic field, eq.(2), where $x = r\cos\theta_B$ and $y = r\sin\theta_B$. Therefore, when $\epsilon_{ha} \neq \epsilon_{ta}$, deeply trapped particle trajectory with the kinetic energy E and the magnetic moment μ is obtained from

$$\sqrt{\epsilon_{ha}^2\frac{x^2+y^2}{a^2} + 2\epsilon_{ha}\epsilon_b\frac{x}{a} + \epsilon_b^2} = 1 - \frac{E}{\mu B_0} - \epsilon_{ta}\frac{x}{a} \quad (4)$$

as

$$(x - X_{dtp})^2 + e^2 y^2 = \rho_{dtp}^2\,, \quad (5)$$

where

$$\begin{aligned} X_{dtp} &\equiv -\frac{\epsilon_{ha}\epsilon_b + \epsilon_{ta}\left(1 - \frac{E}{\mu B_0}\right)}{\epsilon_{ha}^2 - \epsilon_{ta}^2}a\,, \\ e^2 &\equiv \frac{\epsilon_{ha}^2}{\epsilon_{ha}^2 - \epsilon_{ta}^2}\,, \\ \rho_{dtp}^2 &\equiv \frac{\left[\left(1 - \frac{E}{\mu B_0}\right)\epsilon_{ha} + \epsilon_b\epsilon_{ta}\right]^2}{(\epsilon_{ha}^2 - \epsilon_{ta}^2)^2}a^2\,. \end{aligned} \quad (6)$$

Equation (5) shows that mod-B_{min} contours are elliptic with the elongation e when $\epsilon_{ha} > \epsilon_{ta}$, and hyperbola when $\epsilon_{ha} < \epsilon_{ta}$. Particularly, for the case of $\epsilon_{ha} = \epsilon_{ta} \equiv \epsilon_a$, mod-$B_{min}$ contours can be expressed as

$$x = \beta + \gamma y^2, \quad (7)$$

where

$$\begin{aligned} \beta &\equiv \frac{a}{2}\frac{\left(1 - \frac{E}{\mu B_0}\right) - \epsilon_b}{\epsilon_a}\,, \\ \gamma &\equiv -\frac{\epsilon_a}{2a\left[\epsilon_b + \left(1 - \frac{E}{\mu B_0}\right)\right]}\,. \end{aligned} \quad (8)$$

In this case, mod-B_{min} are parabolic and they are not closed. In this paper, the condition $\epsilon_{ha} > \epsilon_{ta}$ is assumed as typically valid for helical-axis heliotrons [1], where mod-B_{min} contours can close.

The closed mod-B_{min} contour exists until it contacts the plasma boundary at $(r/a, \theta_B) =$

$(1,0)$ (outer side of a torus) or $(r/a,\theta_B) = (1,\pi)$ (inner side of a torus) or $\rho_{dtp} = 0$. These conditions lead to the appropriate range of the bumpy field to close the mod-B_{min} contour, depending on $\epsilon_{ta}/\epsilon_{ha}$ and the value of B_{min}. It is noted that $E/(\mu B_0) = B_{min}/B_0$, because deeply trapped particles have zero velocity parallel to magnetic field. In the case of $\epsilon_{ha} > \epsilon_{ta}$, the appropriate range of ϵ_b/ϵ_{ha} to close mod-B_{min} is described as:

$$\frac{B_{min}}{B_0} \le 1-\epsilon_{ha}:$$
$$\text{no closed mod-}B_{min},$$

$$1-\epsilon_{ha} \le \frac{B_{min}}{B_0} \le 1-\epsilon_{ta}:$$
$$\frac{1}{\epsilon_{ha}}\left(1-\frac{B_{min}}{B_0}\right) - 1 - \frac{\epsilon_{ta}}{\epsilon_{ha}} \le \frac{\epsilon_b}{\epsilon_{ha}} \le -\frac{1}{\epsilon_{ha}}\left(1-\frac{B_{min}}{B_0}\right) + 1 - \frac{\epsilon_{ta}}{\epsilon_{ha}},$$
(I) (II)

$$1-\epsilon_{ta} \le \frac{B_{min}}{B_0} \le 1+\frac{\epsilon_b}{\epsilon_{ha}}\epsilon_{ta}:$$
$$-\frac{1}{\epsilon_{ta}}\left(1-\frac{B_{min}}{B_0}\right) \le \frac{\epsilon_b}{\epsilon_{ha}} \le -\frac{1}{\epsilon_{ha}}\left(1-\frac{B_{min}}{B_0}\right) + 1 - \frac{\epsilon_{ta}}{\epsilon_{ha}}.$$
(III) (II)

(9)

The condition (I) arises from the mod-B_{min} contour with B_{min}/B_0 in the range of $1-\epsilon_{ha} \le \frac{B_{min}}{B_0} \le 1-\epsilon_{ta}$ contacts the plasma boundary at $(r/a,\theta_B) = (1,0)$, and (III) from that the mod-B_{min} contour with $1-\epsilon_{ta} \le \frac{B_{min}}{B_0} \le 1+\frac{\epsilon_b}{\epsilon_{ha}}\epsilon_{ta}$ shrinks to $\rho_{dtp} = 0$. The condition (II) gives the contact of the mod-B_{min} contour in the range of $1-\epsilon_{ha} \le \frac{B_{min}}{B_0}$ with the plasma boundary at $(r/a,\theta_B) = (1,\pi)$. As an example, behavior of mod-B_{min} contours is examined for the case of $\epsilon_{ha} = 0.17$ and $\epsilon_{ta}/\epsilon_{ha} = 0.5$. If one considers the mod-B_{min} contour with $B_{min}/B_0 = 0.85$, the appropriate range of ϵ_b/ϵ_{ha} for the closed contour is obtained as

$$-0.618 \le \epsilon_b/\epsilon_{ha} \le -0.382. \qquad (10)$$

Figure 1 shows the mod-B_{min} with $B_{min}/B_0 = 0.85$ for $\epsilon_b/\epsilon_{ha} = -0.618$ (dotted curve) and $\epsilon_b/\epsilon_{ha} = -0.382$ (chain curve). It clearly demonstrates that the mod-B_{min} contour with $B_{min}/B_0 = 0.85$ is shifted in the major radius direction with the bumpy field control. Since the bumpy field can be controlled externally by the toroidal coil currents [1], it can be considered that helical-axis heliotrons have more flexibilty to control the mod-B_{min} structure than conventional planar-axis heliotrons, where the inward magnetic axis shift is typically necessary to improve trapped particle confinement [13].

The above expressions in (9) are plotted in Fig. 2. The horizontal axis denotes the ratio B_{min}/B_0 and vertical one ϵ_b/ϵ_{ha}. Four cases with different $\epsilon_{ta}/\epsilon_{ha}$ are examined here, and $\epsilon_{ta}/\epsilon_{ha} = 0.0, 0.25, 0.5$ and 0.75 cases are shown by solid, dotted, chain and finer dotted lines, respectively. The numbers (I), (II) and (III) on each line correspond to expressions in (9). The mod-B_{min} contours are closed in the region surrounded by the lines for each $\epsilon_{ta}/\epsilon_{ha}$ case. It is seen that the region for the closed mod-B_{min} contours are shifted into negative ϵ_b/ϵ_{ha} region as $\epsilon_{ta}/\epsilon_{ha}$ is increased. This result is understood by considering the change of magnetic field ripple structure as $\epsilon_{ta}/\epsilon_{ha}$ is increased. As $\epsilon_{ta}/\epsilon_{ha}$ is increased, the bottom values of the helicity ($L = 1$)-induced ripples are varied along the magnetic field line due to the toroidicity. This variation can be aligned by the satellite component of the $L = 1$ helical field, which is the $L = 0$ bumpy field as shown in Ref. [14]. For larger $\epsilon_{ta}/\epsilon_{ha}$ cases, larger negative ϵ_b/ϵ_{ha} is required to align the bottom of the

magnetic field ripples.

In conventional heliotrons, the closed mod-B_{min} area is one of the figures of merit to evaluate collisionless particle confinement [15]. Here, it is examined whether this is also valid in helical-axis heliotrons or not. The fraction of the closed mod-B_{min} area to that of the plasma boundary is obtained as:

$$f = \frac{\pi\rho_{dtp}\left(\frac{\rho_{dtp}}{e}\right)}{\pi a^2} = \frac{\left[\left(1 - \frac{B_{min}}{B_0}\right)\epsilon_{ha} + \epsilon_b\epsilon_{ta}\right]^2}{\epsilon_{ha}(\epsilon_{ha}^2 - \epsilon_{ta}^2)^{3/2}}, \tag{11}$$

where $\pi\rho_{dtp}(\rho_{dtp}/e)$ is the closed mod-B_{min} area. It is noted that f increases monotonously as ϵ_b/ϵ_{ha} is varied in the direction from negative value to positive one. This tendency to enlarge the closed mod-B_{min} area is opposite to the closure of mod-B_{min} contour, and therefore, a careful choice of ϵ_b/ϵ_{ha} is essential to a closed mod-B_{min} contour with a sufficient area. Figure 3 shows the dependence of f on ϵ_b/ϵ_{ha} for several cases of $\epsilon_{ta}/\epsilon_{ha}$. Each line denotes the same $\epsilon_{ta}/\epsilon_{ha}$ as in Fig. 2. The maximum value of f for each $\epsilon_{ta}/\epsilon_{ha}$ case is obtained only by the value of ϵ_b/ϵ_{ha} corresponding to the closed mod-B_{min} contour with $B_{min}/B_0 = 1 - \epsilon_{ha}$. It should be noted that the value of ϵ_b/ϵ_{ha}, giving the maximum f for each $\epsilon_{ta}/\epsilon_{ha}$ case, is always negative for $\epsilon_{ta}/\epsilon_{ha} \neq 0$.

To investigate relations between the value of f and collisionless particle confinement, collisionless particle orbits are followed by solving the guiding center equations in the Boozer coordinates [16]. For reference, three configurations **A** ($f = 1$), **B** ($f = 0.866$) and **C** ($f = 0.661$) shown in Fig. 3 are picked up. It is noted that **A** is a helically symmetric configuration. Particle motions of collisionless protons are followed for the average magnetic field strength of 1 T on the magnetic axis. They are launched from magnetic surfaces with $r/a = 0.25, 0.5$ and 0.75 with a uniform distribution in the pitch angle of the velocity space (15 points). The launching points are uniformly distributed in the poloidal (10 points) and toroidal (10 points) angles on each magnetic surface. The number of launched particles from each point is determined by considering the variation of the area element, $dS = J|\nabla\psi|d\theta_B d\zeta_B$ on a magnetic surface [17]. Here, J denotes the Jacobian of the Boozer coordinates. The total number of followed particles is 6105. The proton temperature profile is assumed as $T_i(r/a) = 1.0[1 - (r/a)^2]$ keV. This profile gives the proton energy of 0.9375, 0.75 and 0.4375 keV at the above three radii, respectively. As for reference, 1 keV protons have $\rho_i/a \sim 2.4 \times 10^{-2}$, where ρ_i is the proton Larmor radius. This ratio corresponds to that of 70 keV proton in the W7-X with $a = 0.53$ m and $B_0 = 2.5$ T [9]. The particle orbits are followed for 2 ms. For this period, an 1 keV proton with only parallel velocity initially makes about 80 circuits of a torus. The orbit following is also stopped, when the particle crosses the plasma boundary. This orbit following time is an allowable choice because collisionless particle loss rates almost saturate before 2 ms as shown later. The radial electric field is known to be effective to improve bulk trapped particle confinement in helical systems [1, 15], however; it is less effective for energetic particles such as α particles. Therefore, it is not taken into account in this paper.

Figure 4 shows the time trace of lost particles for three configurations, **A**, **B** and **C**. The fraction of trapped particles for each case is also in-

dicated by the dot. It is noted that all particles are well confined in the configuration **A**. The loss rate is increased as f is decreased (that is, **A** — **B** — **C**). It is noted that the loss rates almost saturate before 2 ms. For example, the loss rate for the configuration **B** increases only 4 % when particles are followed for 6 ms. It is considered from Figs. 3 and 4 that the closed mod-B_{min} area can be utilized to measure global collisionless particle confinement in helical-axis heliotrons as well as in conventional heliotrons. This measure is useful to judge collisionless particle confinement when several helical-axis heliotron configurations are compared.

3 Toroidal Localization of Mod-B_{min} Structure

In the previous section, the bumpy field component has been assumed to be radially constant to make the model magnetic field analytically tractable. However, it is typical to have a radial variation in helical-axis heliotrons [1]. Therefore, roles of radial variation of the bumpy field on collisionless particle confinement is examined in this section for the case with fixed $\epsilon_{ha} = 0.2$ and $\epsilon_{ta}/\epsilon_{ha} = 0.5$. The bumpy field in the model magnetic field (2) is changed as:

$$\epsilon_b \Longrightarrow \epsilon_b[1 + \delta_b(r/a)^2] \,, \qquad (12)$$

where ϵ_b is the bumpy field component on the magnetic axis, and this value is assumed to be the same as in eq.(2). It is interpreted that the radial variation arises from the increase of the bumpy field amplitude towards the plasma edge. It is noted that this type of variation is frequently seen for finite beta equilibria in helical-axis heliotrons.

Figures 5 show the variation of mod-B_{min} as δ_b is increased and each figure includes 4 panels. Here (a) shows the magnetic field spectra in the Boozer coordinates, (b) mod-B_{min} contours projected on a poloidal cross section (that is $((r/a)\cos\theta_B, (r/a)\sin\theta_B)$ plane), (c) mod-B_{min} contours projected on a $(\zeta_B, (r/a)\sin\theta_B)$ plane, respectively. The panel (c) is useful to investigate the toroidal extension of the mod-B_{min} contours. The panel (d) shows the variation of the magnetic field strength $|B|$ on the equatorial line with $\sin\theta_B = 0$ at $\zeta_B = 0$ and $(1/2)(2\pi/M)$.

Figures 5.1 show mod-B_{min} structure for $\delta_b = 0$ case, corresponding to the configuration **B** mentioned above. In this case, the outermost closed mod-B_{min} contour connects $\zeta_B = 0$ and $\zeta_B = (1/2)(2\pi/M)$ as shown in Fig. 5.1(c). This means the existence of the same magnetic field strength at $\zeta_B = 0$ and $\zeta_B = (1/2)(2\pi/M)$ (see Fig. 5.1(d)). As δ_b is increased to 0.5, the magnetic field strength on the equatorial line increases at $\zeta_B = 0$ and decreases at $\zeta_B = (1/2)(2\pi/M)$ with keeping the same strength on the magnetic axis (see Fig. 5.2(d)). The radial width of the outermost closed mod-B_{min} contour is shown by the arrow in Fig. 5.2(d), which connects the same magnetic field strength at $\zeta_B = 0$ and $\zeta_B = (1/2)(2\pi/M)$. The non-closed mod-B_{min} contours have a tendency to localize around $\zeta_B = (1/2)(2\pi/M)$. When δ_b is increased up to 2.0 (this kind of profile of the bumpy field seems possible in finite beta equilibria in helical-axis heliotrons), the magnetic field strength on the equatorial line at $\zeta_B = (1/2)(2\pi/M)$ becomes different from the other two poloidal cross sections. This causes the significant toroidal localization of closed mod-B_{min} contours around $\zeta_B = (1/2)(2\pi/M)$ as in

Figs. 5.3(c) and (d). The required δ_b to localize mod-B_{min} contours around $\zeta_B \sim (1/2)(2\pi/M)$ may be roughly estimated from the profile of magnetic field strength on the equatorial line at $\zeta_B = 0$ and $\zeta_B = (1/2)(2\pi/M)$. The normalized minimum field strength at $\zeta_B = 0$, $B/B_0|_{min,\zeta_B=0}$, is expressed as:

$$1 - \epsilon_b(1+\delta_b) - (\epsilon_{ha} + \epsilon_{ta}) \qquad \left(\delta_b \leq -\frac{\epsilon_{ha}+\epsilon_{ta}}{2\epsilon_b}\right),$$

$$1 - \epsilon_b + \frac{(\epsilon_{ha}+\epsilon_{ta})^2}{4\epsilon_b\delta_b} \qquad \left(\delta_b \geq -\frac{\epsilon_{ha}+\epsilon_{ta}}{2\epsilon_b}\right). \tag{13}$$

On the other hand, the normalized maximum field strength at $\zeta_B = (1/2)(2\pi/M)$, $B/B_0|_{max,\zeta_B=(1/2)(2\pi/M)}$, as:

$$1 + \epsilon_b(1+\delta_b) + (\epsilon_{ha} - \epsilon_{ta}) \qquad \left(\delta_b \geq -\frac{\epsilon_{ha}-\epsilon_{ta}}{2\epsilon_b}\right),$$

$$1 + \epsilon_b - \frac{(\epsilon_{ha}-\epsilon_{ta})^2}{4\epsilon_b\delta_b} \qquad \left(\delta_b \leq -\frac{\epsilon_{ha}-\epsilon_{ta}}{2\epsilon_b}\right). \tag{14}$$

From relations (13) and (14), a condition for δ_b that the minimum magnetic field strength at $\zeta_B = 0$ is larger than the maximum at $\zeta_B = (1/2)(2\pi/M)$ is shown as

$$\delta_b \geq -\frac{(\epsilon_{ha}+\epsilon_{ta}+2\epsilon_b) + \sqrt{2\{(\epsilon_{ha}+\epsilon_b)^2 + (\epsilon_{ta}+\epsilon_b)^2\}}}{2\epsilon_b} \tag{15}$$

which gives $\delta_b \gtrsim 1.2$ for $\epsilon_{ha} = 0.2, \epsilon_{ta} = 0.1$ and $\epsilon_b = -0.1$.

The effect of the localization of closed mod-B_{min} contour on collisionless particle confinement is also examined with the orbit following calculation. Collisionless particle loss rates are compared for different δ_b cases. They are obtained by following 6105 protons with the same assumptions and conditions as used to obtain Fig. 4. Figure 6 shows loss rates for $\delta_b = 0.0, 0.5$ and 2.0, which correspond to configurations shown in Figs. 5.1, 5.2 and 5.3, respectively. It is noted that the closed mod-B_{min} area is the largest for $\delta_b = 0.0$ among three configurations as seen in Figs. 5, and almost similar for both $\delta_b = 0.5$ and 2.0 cases. However, the loss rate is the largest for $\delta_b = 0.0$ case, and significantly reduces as δ_b is increased. This implies that the closed mod-B_{min} area is not a good measure for the collisionless particle confinement when the closed mod-B_{min} contours are toroidally localized.

The reason for this loss rate reduction is investigated from typical trapped particle orbits. Figures 7 show particle orbits with $v_{||} = 0$ initially which are launched from $(r/a, \theta_B) = (0.75, 0.0)$ with $\zeta_B = 0, (1/4)(2\pi/M)$ and $(1/2)(2\pi/M)$ (green, blue and red, respectively). Figure 7.1 is for $\delta_b = 0.0$, Fig. 7.2 for $\delta_b = 1.0$ and Fig. 7.3 for $\delta_b = 2.0$, respectively. The panel (a) shows orbit trajectories projected on the poloidal cross section and panel (b) on (ζ_B, θ_B) plane. The green-colored orbit in Fig. 7.1 is almost deeply trapped particle because its initial point is on the mod-B_{min} (see Fig. 5.1(c)). However, since this starting point is a saddle point of the magnetic field strength, the particle with a non-zero parallel velocity (even much smaller than perpendicular velocity) "slips" and it deviates from the mod-B_{min}. The two other particles (blue and red) in Fig. 7.1 are lost due to the radial drift motion. They are also trapped in the bumpy ripple and do not move toroidal direction largely. However, they have larger parallel velocity than that of green-colored particle, and therefore, they do not follow the mod-B_{min} contour and are quickly lost. As δ_b is increased to 1.0 as shown in Fig. 7.2, closed mod-B_{min} contours localize around

$(1/4)(2\pi/M) \lesssim \zeta_B \lesssim (3/4)(2\pi/M)$. In this case, the particle launched from $\zeta_B = 0$ (green) is not a deeply trapped particle and the trajectory does not reflect the mod-B_{min} structure. The particles from $\zeta_B = (1/4)(2\pi/M)$ and $(1/2)(2\pi/M)$ (blue and red) are toroidally localized around $\zeta_B = (1/2)(2\pi/M)$ as in Fig. 7.2(b) and they almost follow the mod-B_{min} contours. If one increases δ_b further to 2.0 as in Fig. 7.3, closed mod-B_{min} contours are significantly localized as in Fig. 5.3. The particle from $\zeta_B = (1/2)(2\pi/M)$ (red) follows mod-B_{min} because the mod-B_{min} passes through the point $(r/a, \theta_B) = (0.75, 0.0)$. Even the particle started from $\zeta_B = 0$ is completely trapped in the bumpy ripple centered at $\zeta_B = (1/2)(2\pi/M)$, and it repeats bounce motions in the same toroidal field ripple.

Magnetic field topography is also valuable to consider the reason for this improvement with the radial variation of the bumpy field. Figures 8 show the distribution of (a) the magnetic field strength $|B|$, (b) the normalized poloidal derivative of $|B|$, $(1/B)(\partial B/\partial\theta_B)$, and (c) the normalized radial derivative of $|B|$, $(\psi/B)(\partial B/\partial\psi)$ on the $r/a = 0.75$ magnetic surface for one field period. Figure 8.1 is for the configuration with $\delta_b = 0.0$ and Fig. 8.2 for $\delta_b = 2.0$. The latter two quantities strongly affect the particle orbit behavior through the radial and poloidal drift in the Boozer coordinates [16]

$$\dot{\psi} = \frac{\delta}{\gamma}\left(\frac{\partial B}{\partial \zeta_B} I - \frac{\partial B}{\partial \theta_B} g\right),$$

$$\dot{\theta_B} = \frac{g}{\gamma}\left(\delta \frac{\partial B}{\partial \psi} + \epsilon \frac{\partial \Phi}{\partial \psi}\right) - \frac{e^2 B^2}{m} \rho_c \left(\frac{\rho_c g' - \iota}{\gamma}\right),$$

where the same notations as in Ref. [16] are used. When the currentless ($I = 0$), zero beta ($g' = 0$), zero radial electric field ($\Phi = 0$) cases are considered, $\partial B/\partial\theta_B$ ($\partial B/\partial\psi$) contributes to the radial (poloidal) drift directly. The region surrounding the location of B_{min} in Figs. 8.1(a) and 8.2(a) corresponds to the local minimum of the magnetic field strength. This region extends to the entire toroidal field period in Fig. 8.1(a), causing the toroidally connected mod-B_{min} contours in Fig. 5.1. On the other hand, it is toroidally localized as shown in Fig. 8.2(a) for $\delta_b = 2.0$ case, which gives the significant toroidal localization of mod-B_{min} contours in Fig. 5.3. The $|B|$ depends more on the toroidal angle due to the larger bumpy field at $r/a = 0.75$ for $\delta_b = 2.0$ case. The normalized poloidal derivative of $|B|$ shown in Figs. 8.1(b) and 8.2(b) does not alter (except the derivative of $|B|$) by the introduction of the radial variation of the bumpy field, which does not have the poloidal angle dependence. This fact implies that the magnitude of the radial drift is almost the same for these two configurations. The significant difference of the radial derivative of $|B|$ is seen by comparing Figs. 8.1(c) and 8.2(c). The maximum value of $|(\psi/B)(\partial B/\partial\psi)|$ is about 0.1 for $\delta_b = 0.0$ case, and, on the other hand, it is about 0.2 for $\delta_b = 2.0$ case, located at the center of the Fig. 8.2(c). The notable point is that the location of the maximum $|(\psi/B)(\partial B/\partial\psi)|$ is far from the local minimum of $|B|$ for $\delta_b = 0.0$ case, but it is well alinged for $\delta_b = 2.0$ case. Since deeply trapped particles appear around the local minimum of $|B|$, the enhancement of the poloidal drift in the same region for $\delta_b = 2.0$ case effectively reduces the collisionless particle loss as shown in Fig. 6. It should be noted that only the bumpy field can enhance the poloidal drift with keeping the radial drift unchanged by introducing the radial variation of the amplitude, because other dominant field components depend on the

poloidal angle θ_B, which also enhances the radial drift.

These modifications of trapped particle orbits caused by the well alignmenet of the larger poloidal drift region to the region of local minimum of the magnetic field strength cause the improvement of collisionless particle confinement. This is realized by the introduction of the increase of the bumpy field towards the plasma edge, which may be obtained in finite beta equilibria in helical-axis heliotrons. At zero beta, the control of toroidal coil current will produce such profile of the bumpy field. Thus the bumpy field is worth for improving collisionless particle confinement in helical-axis heliotrons with the flexibility for the bumpy field control.

4 Summary

Roles of bumpy field on collisionless particle confinement in helical-axis heliotrons have been considered based on the mod-B_{min} structure and orbit calculations in the Boozer coordinates. The typical model magnetic field for conventional planar-axis heliotrons include only helicity and toroidicity components in the Boozer spectrum. However, since the bumpy field component typically appears in helical-axis heliotrons, the model magnetic field has been extended to include it.

Mod-B_{min} contours projected on a poloidal cross section become elliptic shape depending on the ratio between the toroidicity and helicity. The center of mod-B_{min} contour can be shifted with the bumpy field. Thus helical-axis heliotrons have a larger flexibility to control the mod-B_{min} structure than conventional planar-axis heliotrons. Therefore, the inward magnetic axis shift, which is usually required to align the mod-B_{min} contours with magnetic surfaces in conventional heliotrons, is not necessarily essential in helical-axis heliotrons. This property is favorable to obtain the compatibility between sufficient MHD properties and good particle confinement. The conditions for the existence of the closed mod-B_{min} contours lead to the appropriate range of the ratio of ϵ_b/ϵ_h depending on the B_{min} value or the particle energy. It becomes more negative as the ratio of ϵ_t/ϵ_h is increased. This negative value of ϵ_b/ϵ_h is required to align the bottom of the magnetic field ripple, which is necessary to close mod-B_{min} contours. According to the orbit following calculations, collisionless particle loss rate is decreased as the closed mod-B_{min} area projected on the poloidal cross section is increased. Therefore, the closed mod-B_{min} area can be utilized as the measure to evaluate the collisionless particle confinement as long as the mod-B_{min} contours extend throughout a torus.

Mod-B_{min} contours are toroidally localized when the bumpy field amplitude is increased towards the plasma edge. This is due to the formation of local minimum of the magnetic field strength around the toroidal angle where the bumpy field contributes to weaken the field strength. The orbit calculations show the significant improvement of collisionless particle confinement in the presence of toroidally localized mod-B_{min} contours. The collisionless particles with almost only perpendicular velocity follow these toroidally localized mod-B_{min} contours in one field period after being trapped in the bumpy field ripple. This occurs even if they are launched from the toroidal angle where mod-B_{min} contours

do not pass, which is the main reason for the significant improvement. The magnetic field topography is also valuable to consider the reason for the improvement. The region with the large poloidal drift is well alinged to the region of the local minimum of the magnetic field strength with keeping the radial drift unchanged for the configuration with the radially increasing bumpy field. The bumpy field is the only field component without the poloidal dependence, which does not induce the radial drift even if the radial variation of the amplitude is introduced. Since the bumpy field component can be controlled in a wide range through the coil current control in helical-axis heliotrons, it should be worth investigating a suitable coil current distribution based on this study.

Acknowledgements

One of authors (M.Y.) gratefully acknowledges productive and fruitful discussions with Prof. J. Nührenberg and Dr. S. Murakami. Continuous encouragements from Prof. F. Sano are also appreciated. This work has been supported by grant-in-aid from Ministry of Education, Science and Culture (Monbusho), Japan.

References

[1] YOKOYAMA, M., NAKAMURA, Y., WAKATANI, M., J. Plasma Phys. Fusion Res. **73** (1997) 723.

[2] WAKATANI, M., et al., in Proc. 17th Int. Conf. on Plasma Physics and Controlled Nuclear Fusion Research, 1998, Yokohama, (in press)

[3] UO, K., et al., in Proc. 8th Int. Conf. on Plasma Physics and Controlled Nuclear Fusion Research, 1980, Brussels, (IAEA Vienna 1981) Vol.1, p.217.

[4] IIYOSHI, A., et al., Fusion Technol. **17** (1990) 169.

[5] OBIKI, T., et al., in Proc. 13th Int. Conf. on Plasma Physics and Controlled Nuclear Fusion Research, 1990, Washington, D. C., (IAEA Vienna 1991) Vol.2, p.425.

[6] OBIKI, T., et al., in Proc. 14th Int. Conf. on Plasma Physics and Controlled Nuclear Fusion Research, 1992, Würzburg, (IAEA Vienna 1993) Vol.2, p.403.

[7] HAYASHI, T., et al., Phys. Fluids **B4** (1992) 1539.

[8] SANUKI, H., TODOROKI, J., KAMIMURA, T., Phys. Fluids **B2** (1990) 2155.

[9] GRIEGER, G et al., Phys. Fluids **B4** (1992) 2081.

[10] PAINTER, S. L., GARDNER, H. J., Nucl. Fusion **33** (1993) 1107.

[11] BOOZER, A. H., Phys. Fluids **23**(1980)904.

[12] SHAING, K. C., HOKIN, S. A., Phys. Fluids **26** (1983) 2136.

[13] TODOROKI, J., et al., in Proc. 12th Int. Conf. on Plasma Physics and Controlled Nuclear Fusion Research, 1988, Nice (IAEA Vienna 1989) Vol.2, p.637.

[14] MYNICK, H. E., et al., Phys. Rev. Lett. **48** (1982) 322.

[15] KATO, A., NAKAMURA, Y., WAKATANI, M., J. Phys. Soc. Jpn. **60** (1991) 494.

[16] FOWLER, R. H., et al., Phys. Fluids **28** (1985) 338.

[17] NAKAJIMA, N., Phys. Plasmas **3** (1996) 4545.

Figure Captions

Fig. 1: Mod-B_{min} with $B_{min}/B_0 = 0.85$ for $\epsilon_b/\epsilon_{ha} = -0.618$ (dotted curve) and $\epsilon_b/\epsilon_{ha} = -0.382$ (chain curve) in the case of $\epsilon_{ha} = 0.17$ and $\epsilon_{ta}/\epsilon_{ha} = 0.5$.

Fig. 2: The range of ϵ_b/ϵ_{ha} to close the mod-B_{min} contour in the range of $0.8 \leq B_{min}/B_0 \leq 0.95$ in the cases of $\epsilon_{ta}/\epsilon_{ha} = 0.0, 0.25, 0.5$ and 0.75 (solid, dotted, chain and finer dotted line, respectively) with $\epsilon_{ha} = 0.2$. The numbers (I), (II) and (III) on each line correspond to those in (9).

Fig. 3: The fraction of closed mod-B_{min} area to the plasma cross section, f, as a function of ϵ_b/ϵ_{ha} for several cases of $\epsilon_{ta}/\epsilon_{ha}$. Each line denotes the same $\epsilon_{ta}/\epsilon_{ha}$ as in Fig. 2.

Fig. 4: Time trace of lost particles for three configurations, **A**, **B** and **C** indicated in Fig. 3. The fraction of trapped particles for each case is also indicated by the dot.

Fig. 5.1-3: **(a)** Magnetic field spectra in the Boozer coordinates for $\epsilon_{ta}/\epsilon_{ha} = 0.5$ and $\epsilon_b/\epsilon_{ha} = -0.5$. **(b)** Mod-$B_{min}$ contours projected on a poloidal cross section. **(c)** Mod-B_{min} contours projected on a $(\zeta_B, (r/a)\sin\theta_B)$ plane. **(d)** The variation of the magnetic field strength $|B|$ on the equatorial line on $\zeta_B = 0$ and $(1/2)(2\pi/M)$.

Fig. 6: Time trace of lost particles for three configurations with several δ_b values. The fraction of trapped particles is also indicated by the dot.

Fig. 7: **(a)** Poloidal projection of collisionless particle orbits with $v_{\|} = 0$ initially in the configuration with $\epsilon_{ta}/\epsilon_{ha} = 0.5$, $\epsilon_b/\epsilon_{ha} = -0.5$, and $\delta_b = 0.0$ (Fig. 7.1), $\delta_b = 1.0$ (Fig. 7.2) and $\delta_b = 2.0$ (Fig. 7.3). They are launched from $(r/a, \theta_B) = (0.75, 0.0)$ with $\zeta_B = 0, (1/4)(2\pi/M)$ and $(1/2)(2\pi/M)$ (green, blue and red, respectively). **(b)** Particle trajectory on (ζ_B, θ_B) plane for the corresponding particles shown in panel (a).

Fig. 8.1-2: The distribution of **(a)** the magnetic field strength $|B|$, **(b)** the normalized poloidal derivative of $|B|$, $(1/B)(\partial B/\partial\theta_B)$, and **(c)** the normalized radial derivative of $|B|$, $(\psi/B)(\partial B/\partial\psi)$ on the $r/a = 0.75$ magnetic surface for one field period.

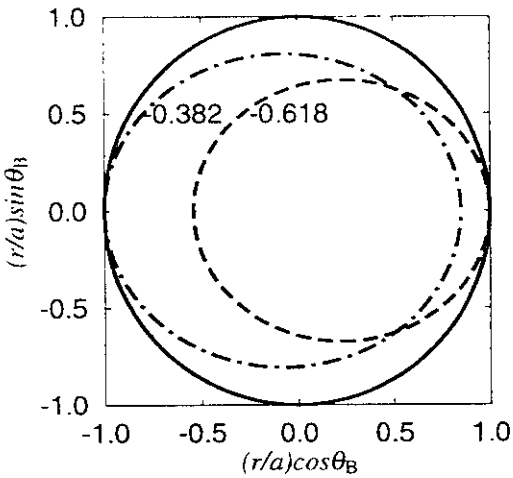

Fig. 1

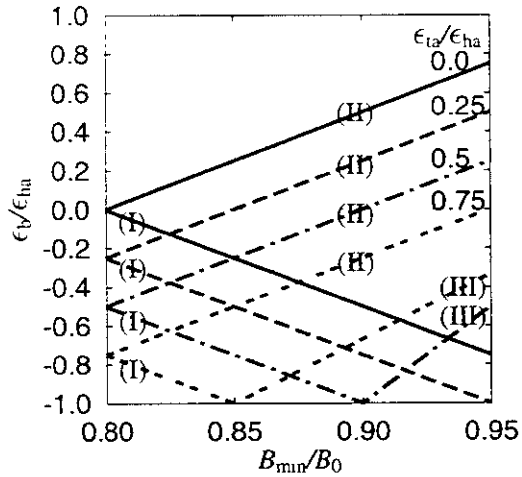

Fig. 2

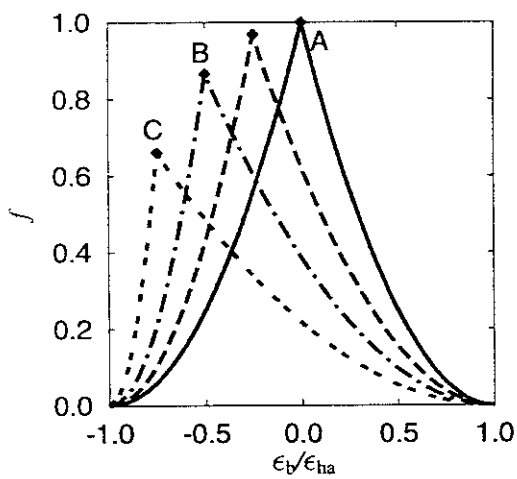

Fig. 3

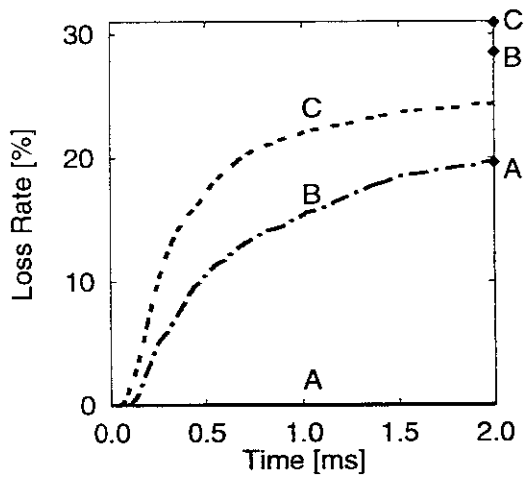

Fig. 4

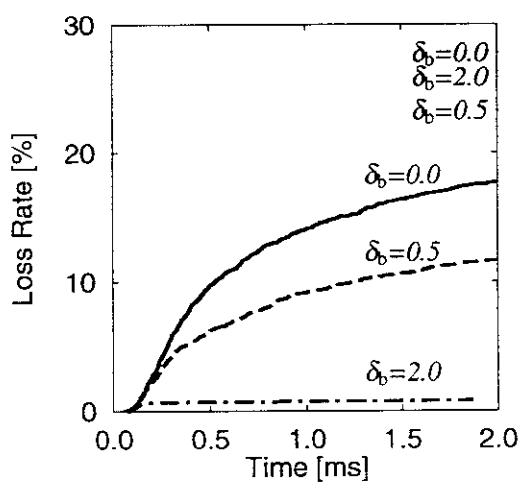

Fig. 6

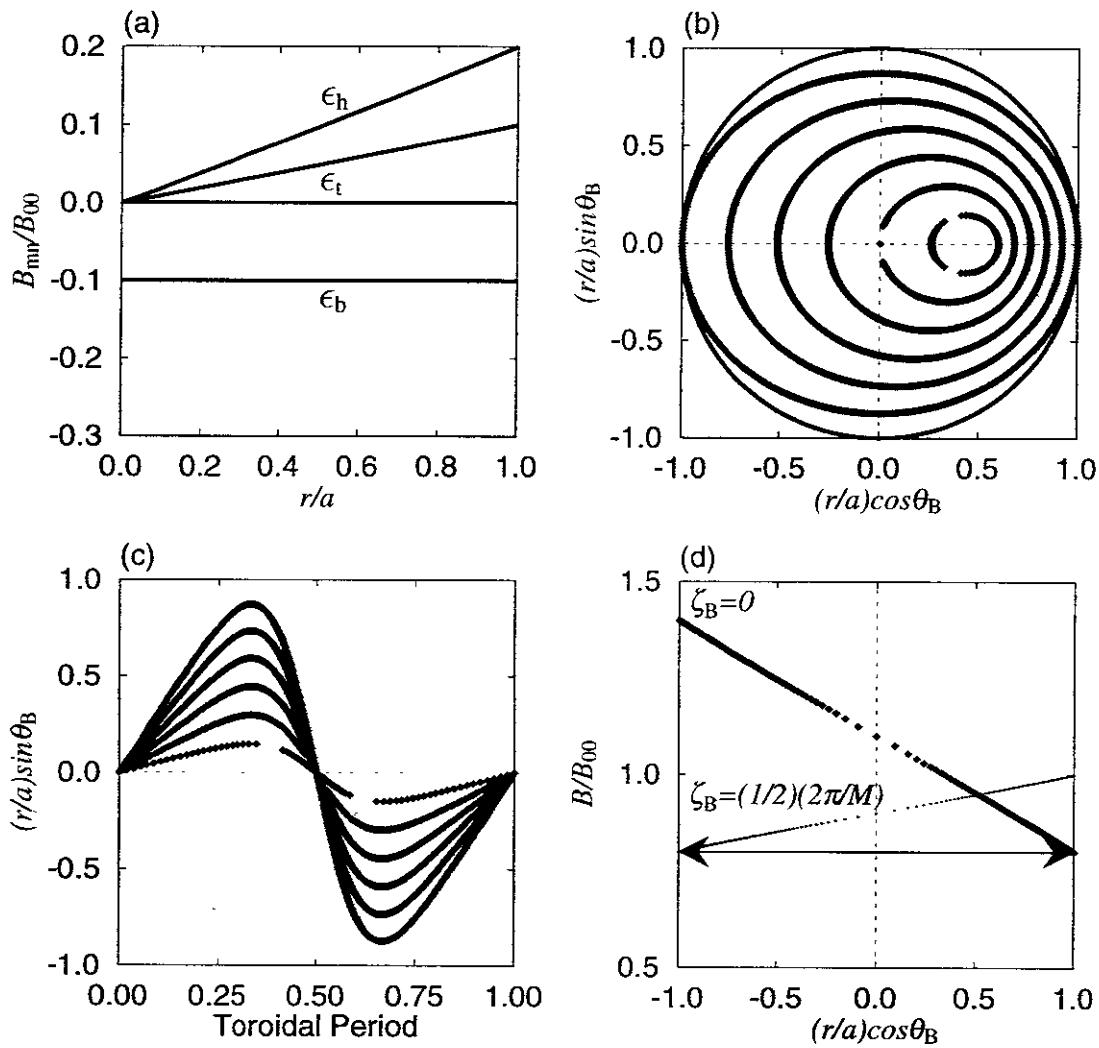
(a)
0.2
0.1
0.0
-0.1
-0.2
-0.3
ϵ_h
ϵ_t
ϵ_b
B_{min}/B_{00}
0.0 0.2 0.4 0.6 0.8 1.0
r/a
(b)
1.0
0.5
0.0
-0.5
-1.0
$(r/a)sin\theta_B$
-1.0 -0.5 0.0 0.5 1.0
$(r/a)cos\theta_B$
(c)
1.0
0.5
0.0
-0.5
-1.0
$(r/a)sin\theta_B$
0.00 0.25 0.50 0.75 1.00
Toroidal Period
(d)
1.5
1.0
0.5
$\zeta_B=0$
$\zeta_B=(1/2)(2\pi/M)$
B/B_{00}
-1.0 -0.5 0.0 0.5 1.0
$(r/a)cos\theta_B$

Fig. 5.1

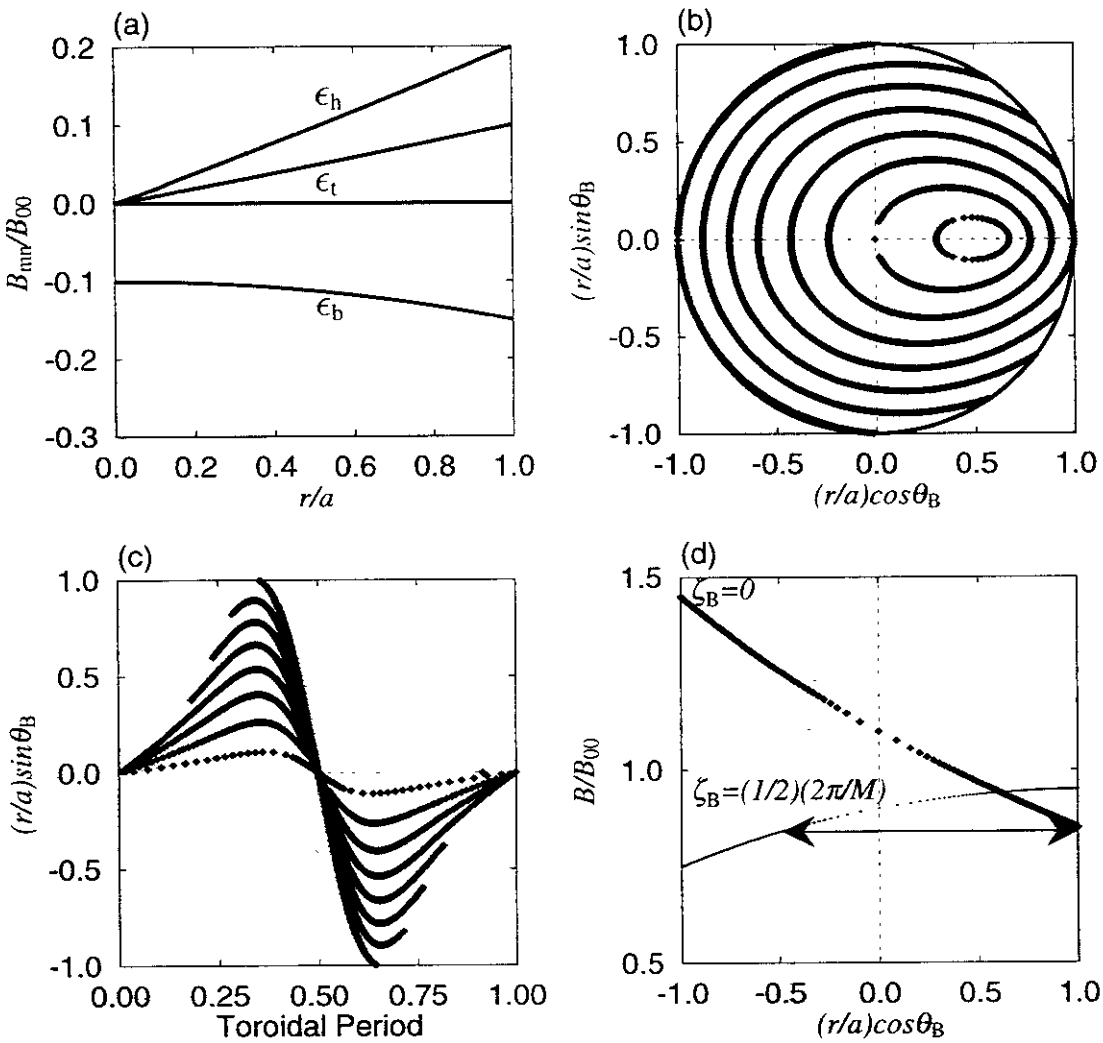
(a)
0.2
0.1
0.0
-0.1
-0.2
-0.3
ϵ_h
ϵ_t
ϵ_b
B_{min}/B_{00}
0.0 0.2 0.4 0.6 0.8 1.0
r/a
(b)
1.0
0.5
0.0
-0.5
-1.0
$(r/a)sin\theta_B$
-1.0 -0.5 0.0 0.5 1.0
$(r/a)cos\theta_B$
(c)
1.0
0.5
0.0
-0.5
-1.0
$(r/a)sin\theta_B$
0.00 0.25 0.50 0.75 1.00
Toroidal Period
(d)
1.5
1.0
0.5
B/B_{00}
$\zeta_B=0$
$\zeta_B=(1/2)(2\pi/M)$
-1.0 -0.5 0.0 0.5 1.0
$(r/a)cos\theta_B$

Fig. 5.2

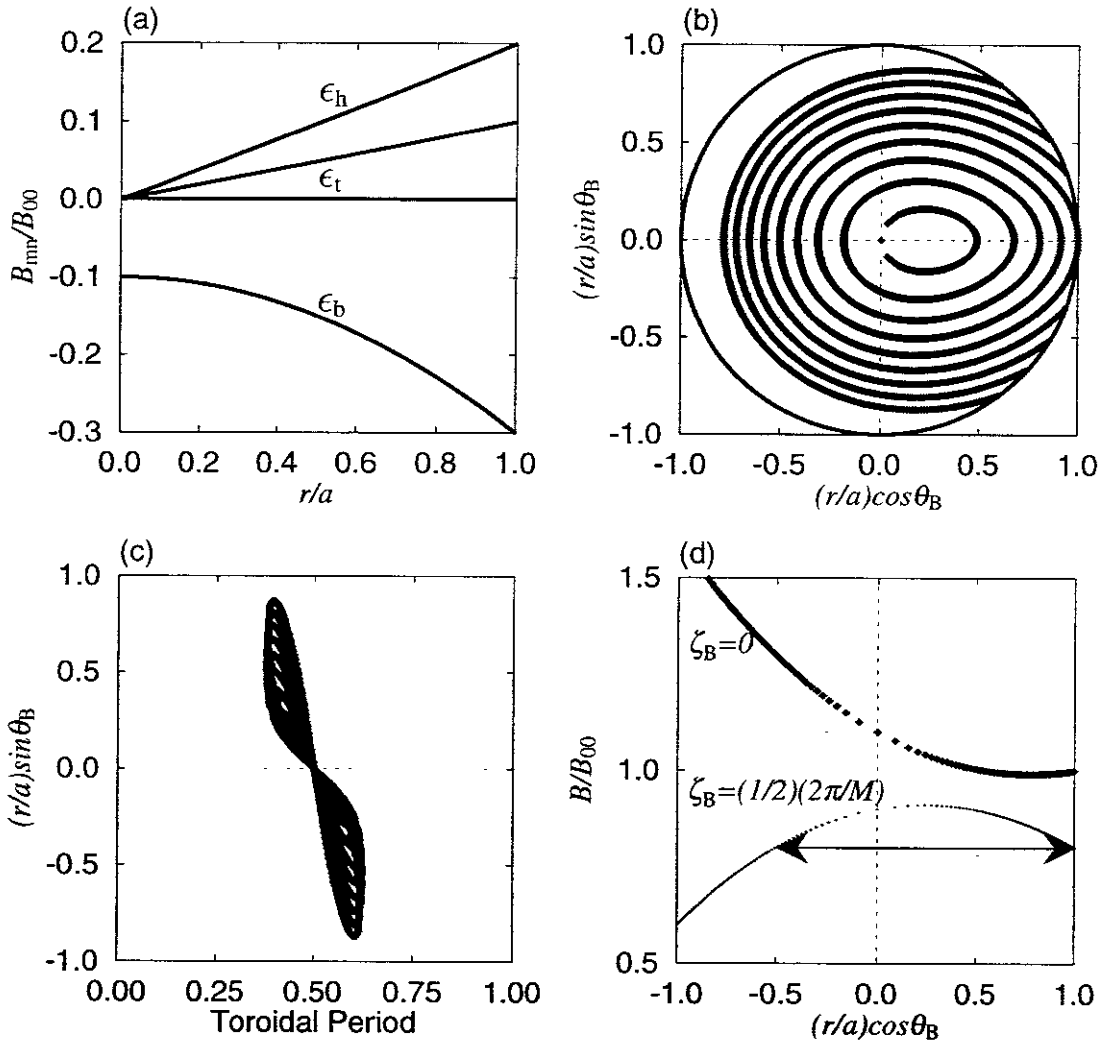
(a)
0.2
0.1
0.0
-0.1
-0.2
-0.3
B_{mn}/B_{00}
ϵ_h
ϵ_t
ϵ_b
0.0 0.2 0.4 0.6 0.8 1.0
r/a
(b)
1.0
0.5
0.0
-0.5
-1.0
$(r/a)sin\theta_B$
-1.0 -0.5 0.0 0.5 1.0
$(r/a)cos\theta_B$
(c)
1.0
0.5
0.0
-0.5
-1.0
$(r/a)sin\theta_B$
0.00 0.25 0.50 0.75 1.00
Toroidal Period
(d)
1.5
1.0
0.5
B/B_{00}
$\zeta_B=0$
$\zeta_B=(1/2)(2\pi/M)$
-1.0 -0.5 0.0 0.5 1.0
$(r/a)cos\theta_B$

Fig. 5.3

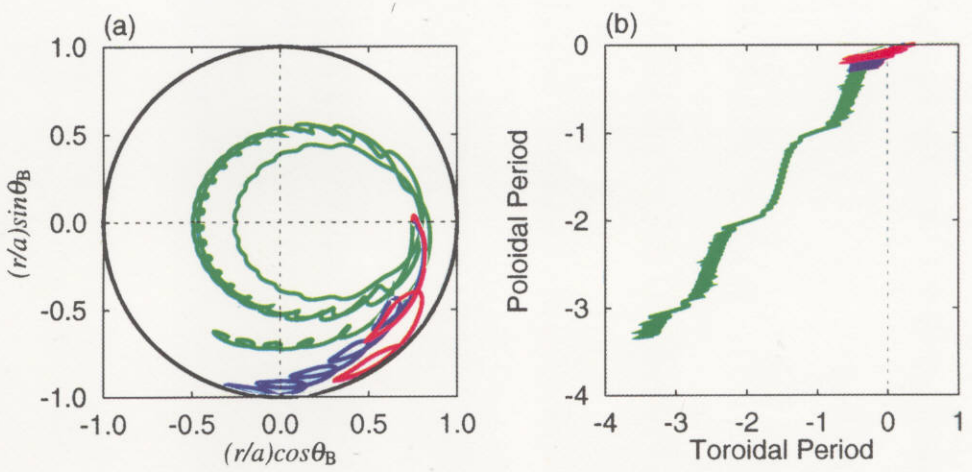

Fig. 7.1

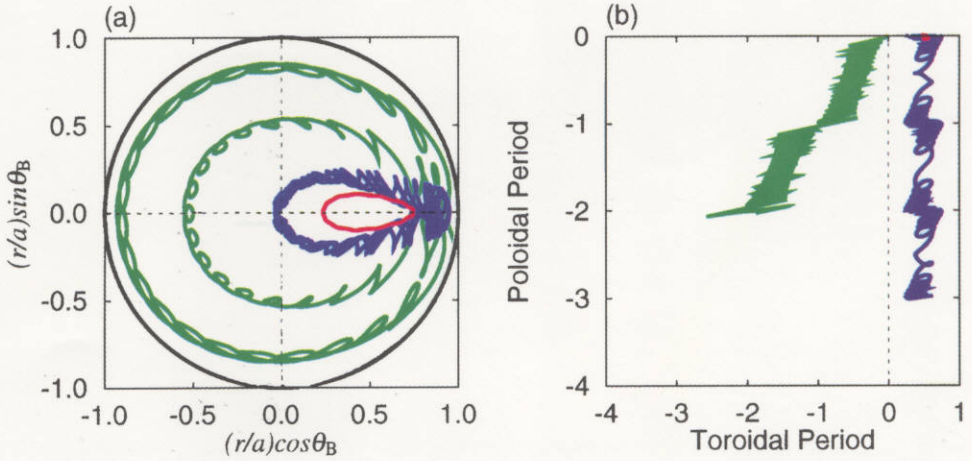

Fig. 7.2

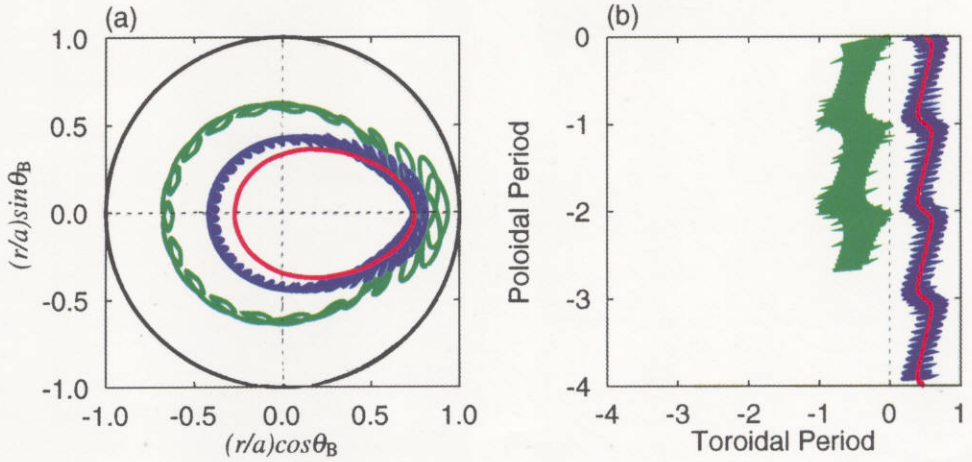

Fig. 7.3

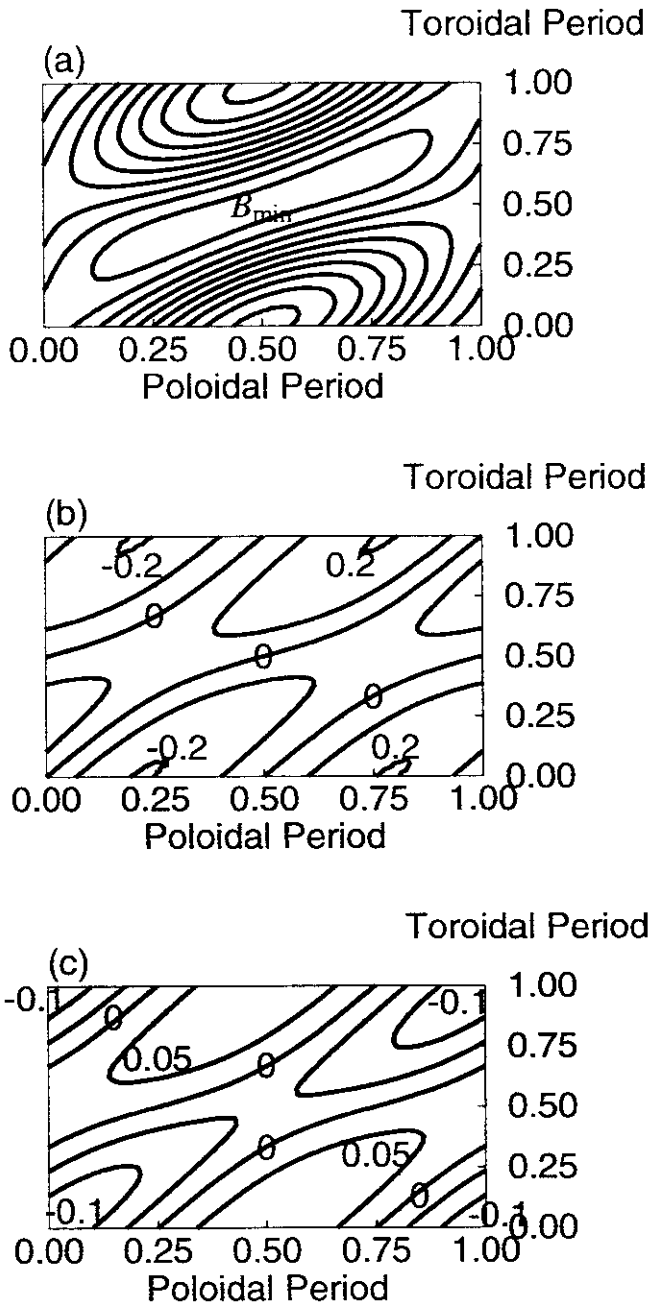
Toroidal Period
(a)
1.00
0.75
0.50
0.25
0.00
B_{min}
0.00 0.25 0.50 0.75 1.00
Poloidal Period
Toroidal Period
(b)
1.00
0.75
0.50
0.25
0.00
-0.2
0.2
0
0
0
-0.2
0.2
0.00 0.25 0.50 0.75 1.00
Poloidal Period
Toroidal Period
(c)
1.00
0.75
0.50
0.25
0.00
-0.1
-0.1
0
0.05
0
0
0.05
0
-0.1
-0.1
0.00 0.25 0.50 0.75 1.00
Poloidal Period

Fig. 8.1

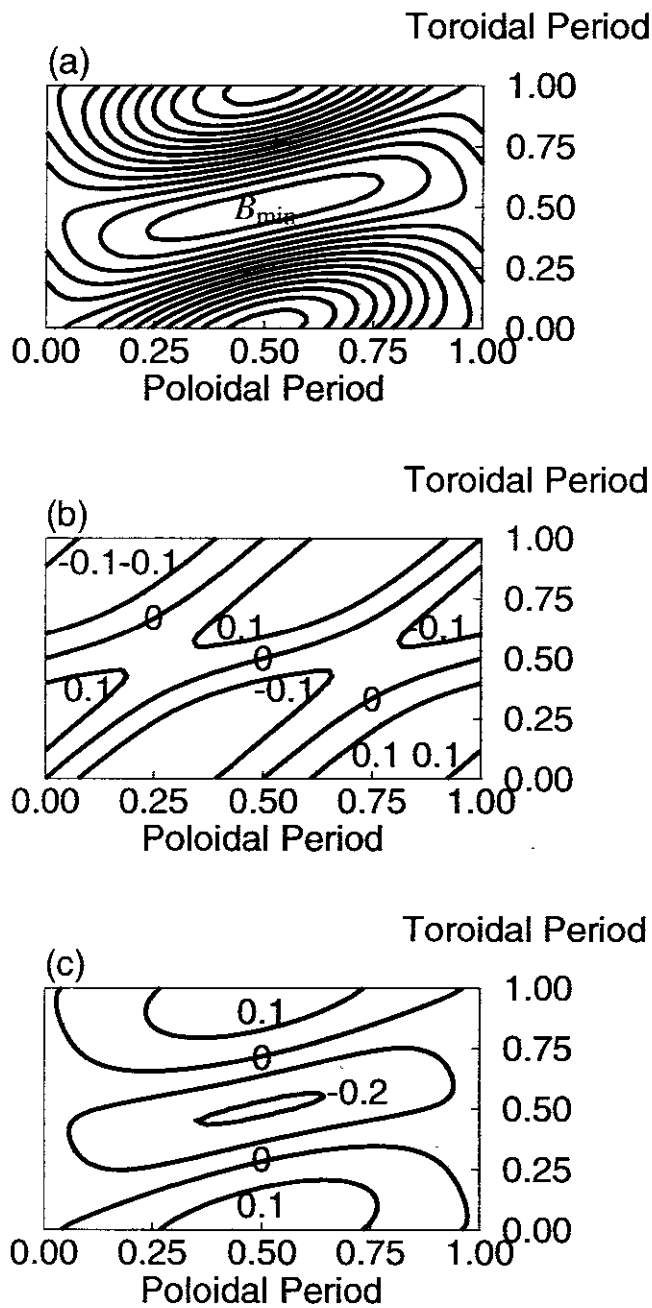
Toroidal Period
(a)
1.00
0.75
0.50
0.25
0.00
B_{min}
0.00 0.25 0.50 0.75 1.00
Poloidal Period
Toroidal Period
(b)
-0.1-0.1
0
0.1
-0.1
0
0.1
-0.1
0
0.1 0.1
1.00
0.75
0.50
0.25
0.00
0.00 0.25 0.50 0.75 1.00
Poloidal Period
Toroidal Period
(c)
0.1
0
-0.2
0
0.1
1.00
0.75
0.50
0.25
0.00
0.00 0.25 0.50 0.75 1.00
Poloidal Period

Fig. 8.2

Recent Issues of NIFS Series

NIFS-519 M Yokoyama, N. Nakajima and M Okamoto,
Nonlinear Incompressible Poloidal Viscosity in L=2 Heliotron and Quasi-Symmetric Stellarators; Nov 1997

NIFS-520 S Kida and H. Miura,
Identificaiton and Analysis of Vortical Structures, Nov 1997

NIFS-521 K. Ida, S. Nishimura, T. Minami, K. Tanaka, S Okamura, M. Osakabe, H. Idei, S Kubo, C Takahashi and K. Matsuoka,
High Ion Temperature Mode in CHS Heliotron/torsatron Plasmas, Nov. 1997

NIFS-522 M. Yokoyama, N Nakajima and M Okamoto,
Realization and Classification of Symmetric Stellarator Configurations through Plasma Boundary Modulations, Dec. 1997

NIFS-523 H Kitauchi,
Topological Structure of Magnetic Flux Lines Generated by Thermal Convection in a Rotating Spherical Shell; Dec. 1997

NIFS-524 T. Ohkawa,
Tunneling Electron Trap; Dec. 1997

NIFS-525 K. Itoh, S.-I. Itoh, M. Yagi, A. Fukuyama,
Solitary Radial Electric Field Structure in Tokamak Plasmas; Dec. 1997

NIFS-526 Andrey N Lyakhov,
Alfven Instabilities in FRC Plasma, Dec 1997

NIFS-527 J. Uramoto,
Net Current Increment of negative Muonlike Particle Produced by the Electron and Positive Ion Bunch-method, Dec. 1997

NIFS-528 Andrey N. Lyakhov,
Comments on Electrostastic Drift Instabilities in Field Reversed Configuraiton; Dec. 1997

NIFS-529 J. Uramoto,
Pair Creation of Negative and Positive Pionlike (Muonlike) Particle by Interaction between an Electron Bunch and a Positive Ion Bunch; Dec. 1997

NIFS-530 J. Uramoto,
Measuring Method of Decay Time of Negative Muonlike Particle by Beam Collector Applied RF Bias Voltage; Dec. 1997

NIFS-531 J Uramoto,
Confirmation Method for Metal Plate Penetration of Low Energy Negative Pionlike or Muonlike Particle Beam under Positive Ions, Dec. 1997

NIFS-532 J. Uramoto,
Pair Creations of Negative and Positive Pionlike (Muonlike) Particle or K Mesonlike (Muonlike) Particle in H2 or D2 Gas Discharge in Magnetic Field; Dec. 1997

NIFS-533 S. Kawata, C. Boonmee, T. Teramoto, L. Drska, J. Limpouch, R. Liska, M. Sinor,
Computer-Assisted Particle-in-Cell Code Development; Dec. 1997

NIFS-534 Y. Matsukawa, T Suda, S. Ohnuki and C. Namba,
Microstructure and Mechanical Property of Neutron Irradiated TiNi Shape Memory Alloy; Jan. 1998

NIFS-535 A. Fujisawa, H. Iguchi, H Idei, S. Kubo, K. Matsuoka, S. Okamura, K Tanaka, T Minami, S. Ohdachi, S Morita, H. Zushi, S Lee, M Osakabe, R. Akiyama, Y. Yoshimura, K. Toi, H. Sanuki, K Itoh, A Shimizu, S Takagi, A. Ejiri, C. Takahashi, M. Kojima, S. Hidekuma, K Ida, S. Nishimura, N Inoue, R Sakamoto, S.-I Itoh, Y Hamada, M. Fujiwara,
Discovery of Electric Pulsation in a Toroidal Helical Plasma, Jan 1998

NIFS-536 Lj.R. Hadzievski, M.M. Skoric, M. Kono and T. Sato,
Simulation of Weak and Strong Langmuir Collapse Regimes; Jan. 1998

NIFS-537 H. Sugama, W Horton,
Nonlinear Electromagnetic Gyrokinetic Equation for Plasmas with Large Mean Flows; Feb 1998

NIFS-538 H. Iguchi, T.P Crowley, A. Fujisawa, S Lee, K. Tanaka, T. Minami, S. Nishimura, K. Ida, R. Akiyama, Y Hamada, H., Idei, M Isobe, M. Kojima, S. Kubo, S. Monta, S. Ohdachi, S. Okamura, M. Osakabe, K. Matsuoka, C. Takahashi and K. Toi,
Space Potential Fluctuations during MHD Activities in the Compact Helical System (CHS); Feb 1998

NIFS-539 Takashi Yabe and Yan Zhang,
Effect of Ambient Gas on Three-Dimensional Breakup in Coronet Formation Process; Feb. 1998

NIFS-540 H. Nakamura, K. Ikeda and S. Yamaguchi,
Transport Coefficients of InSb in a Strong Magnetic Field; Feb. 1998

NIFS-541 J. Uramoto,
Development of ν_μ Beam Detector and Large Area ν_μ Beam Source by H_2 Gas Discharge (I); Mar. 1998

NIFS-542 J. Uramoto,
Development of $bar{\nu}_\mu$ Beam Detector and Large Area $bar{\nu}_\mu$ Beam Source by H_2 Gas Discharge (II); Mar. 1998

NIFS-543 J. Uramoto,
Some Problems inside a Mass Analyzer for Pions Extracted from a H_2 Gas Discharge; Mar. 1998

NIFS-544 J. Uramoto,
Simplified ν_μ $bar{\nu}_\mu$ Beam Detector and ν_μ $bar{\nu}_\mu$ Beam Source by Interaction between an Electron Bunch and a Positive Ion Bunch, Mar 1998

NIFS-545 J. Uramoto,
Various Neutrino Beams Generated by D_2 Gas Discharge; Mar.1998

NIFS-546 R. Kanno, N. Nakajima, T. Hayashi and M. Okamoto,
Computational Study of Three Dimensional Equilibria with the Bootstrap Current; Mar. 1998

NIFS-547 R. Kanno, N. Nakajima and M. Okamoto,
Electron Heat Transport in a Self-Similar Structure of Magnetic Islands; Apr. 1998

NIFS-548 J.E. Rice,
Simulated Impurity Transport in LHD from MIST; May 1998

NIFS-549 M.M. Skoric, T. Sato, A.M. Maluckov and M.S. Jovanovic,
On Kinetic Complexity in a Three-Wave Interaction; June 1998

NIFS-550 S. Goto and S Kida,
Passive Saclar Spectrum in Isotropic Turbulence: Prediction by the Lagrangian Direct-interaction Approximation; June 1998

NIFS-551 T. Kuroda, H Sugama, R. Kanno, M. Okamoto and W. Horton,
Initial Value Problem of the Toroidal Ion Temperature Gradient Mode ; June 1998

NIFS-552 T. Mutoh, R. Kumazawa, T. Seki, F. Simpo, G. Nomura, T. Ido and T Watari,
Steady State Tests of High Voltage Ceramic Feedthoughs and Co-Axial Transmission Line of ICRF Heating System for the Large Helical Device ; June 1998

NIFS-553 N. Noda, K. Tsuzuki, A. Sagara, N. Inoue, T. Muroga,
oronaization in Future Devices -Protecting Layer against Tritium and Energetic Neutrals-: July 1998

NIFS-554 S. Murakami and H. Saleem,
Electromagnetic Effects on Rippling Instability and Tokamak Edge Fluctuations; July 1998

NIFS-555 H. Nakamura, K. Ikeda and S. Yamaguchi,
Physical Model of Nernst Element; Aug. 1998

NIFS-556 H Okumura, S Yamaguchi, H Nakamura K Ikeda and K Sawada,
Numerical Computation of Thermoelectric and Thermomagnetic Effects, Aug 1998

NIFS-557 Y Takeiri, M Osakabe, K Tsumori Y Oka, O Kaneko, E Asano, T Kawamoto, R Akiyama and M Tanaka,
Development of a High-Current Hydrogen-Negative Ion Source for LHD-NBI System, Aug 1998

NIFS-558 M Tanaka, A Yu Grosberg and T Tanaka,
Molecular Dynamics of Structure Organization of Polyampholytes; Sep 1998

NIFS-559 R Horiuchi, K Nishimura and T Watanabe
Kinetic Stabilization of Tilt Disruption in Field-Reversed Configurations; Sep. 1998
(IAEA-CN-69/THP1/11)

NIFS-560 S Sudo, K. Kholopenkov, K Matsuoka, S Okamura, C Takahashi, R. Akiyama, A Fujisawa, K Ida, H Idei, H Iguchi, M Isobe, S Kado, K Kondo, S Kubo, H Kuramoto, T Minami, S Morita, S Nishimura, M Osakabe, M. Sasao, B Peterson, K. Tanaka, K Toi and Y. Yoshimura,
Particle Transport Study with Tracer-Encapsulated Solid Pellet Injection; Oct 1998
(IAEA-CN-69/EXP1/18)

NIFS-561 A Fujisawa, H Iguchi, S Lee, K Tanaka, T Minami, Y. Yoshimura, M. Osakabe, K. Matsuoka, S Okamura, H. Idei, S. Kubo, S Ohdachi S Morita, R Akiyama, K. Toi H Sanuki, K Itoh, K Ida, A. Shimizu, S Takagi, C. Takahashi, M Kojima, S. Hidekuma, S Nishimura, M. Isobe, A Ejiri, N. Inoue, R Sakamoto, Y Hamada and M Fujiwara,
Dynamic Behavior Associated with Electric Field Transitions in CHS Heliotron/Torsatron, Oct 1998
(IAEA-CN-69/EX5/1)

NIFS-562 S Yoshikawa,
Next Generation Toroidal Devices, Oct 1998

NIFS-563 Y Todo and T. Sato,
Kinetic-Magnetohydrodynamic Simulation Study of Fast Ions and Toroidal Alfvén Eigenmodes; Oct 1998
(IAEA-CN-69/THP2/22)

NIFS-564 T Watari, T Shimozuma, Y. Takeiri, R. Kumazawa, T. Mutoh, M. Sato, O Kaneko, K. Ohkubo, S. Kubo, H. Idei, Y. Oka, M. Osakabe, T Seki, K. Tsumori, Y. Yoshimura, R Akiyama, T. Kawamoto, S. Kobayashi, F. Shimpo, Y Takita, E. Asano, S. Itoh, G Nomura, T Ido, M Hamabe, M Fujiwara, A Iiyoshi, S Morimoto, T. Bigelow and Y P Zhao,
Steady State Heating Technology Development for LHD; Oct. 1998
(IAEA-CN-69/FTP/21)

NIFS-565 A Sagara, K Y. Watanabe, K Yamazaki, O Motojima, M Fujiwara, O. Mitarai, S Imagawa, H. Yamanishi, H Chikaraishi, A Kohyama, H Matsui, T Muroga, T. Noda, N. Ohyabu, T Satow, A.A Shishkin, S. Tanaka, T Terai and T. Uda,
LHD-Type Compact Helical Reactors; Oct 1998
(IAEA-CN-69/FTP/03(R)

NIFS-566 N. Nakajima, J. Chen, K Ichiguchi and M Okamoto,
Global Mode Analysis of Ideal MHD Modes in L=2 Heliotron/Torsatron Systems, Oct 1998
(IAEA-CN-69/THP1/08)

NIFS-567 K. Ida, M Osakabe, K Tanaka, T. Minami, S Nishimura, S Okamura, A Fujisawa, Y. Yoshimura, S. Kubo, R. Akiyama, D.S Darrow, H Idei, H. Iguchi, M. Isobe, S. Kado, T. Kondo, S. Lee, K. Matsuoka, S. Morita, I Nomura, S Ohdachi, M Sasao, A. Shimizu, K. Tumori, S. Takayama, M Takechi, S Takagi, C Takahashi, K. Toi and T Watari,
Transition from L Mode to High Ion Temperature Mode in CHS Heliotron/Torsatron Plasmas; Oct 1998
(IAEA-CN-69/EX2/2)

NIFS-568 S Okamura, K. Matsuoka, R Akiyama, D S. Darrow, A Ejiri, A. Fujisawa, M Fujiwara, M Goto, K. Ida H. Idei, H Iguchi, N. Inoue, M Isobe, K Itoh, S Kado, K Kholopenkov, T Kondo, S. Kubo, A. Lazaros, S. Lee, G Matsunaga, T. Minami, S. Morita, S. Murakami, N. Nakajima, N Nikai, S Nishimura, I. Nomura, S Ohdachi, K. Ohkuni, M Osakabe, R. Pavlichenko, B Peterson, R. Sakamoto, H. Sanuki, M. Sasao, A. Shimizu, Y Shirai, S Sudo, S. Takagi, C Takahashi, S Takayama, M Takechi, K Tanaka, K Toi, K Yamazaki, Y. Yoshimura and T Watari,
Confinement Physics Study in a Small Low-Aspect-Ratio Helical Device CHS, Oct 1998
(IAEA-CN-69/OV4/5)

NIFS-569 M M Skoric, T. Sato, A. Maluckov, M S Jovanovic,
Micro- and Macro-scale Self-organization in a Dissipative Plasma, Oct 1998

NIFS-570 T Hayashi, N Mizuguchi, T-H. Watanabe, T Sato and the Complexity Simulation Group,
Nonlinear Simulations of Internal Reconnection Event in Spherical Tokamak, Oct 1998
(IAEA-CN-69/TH3/3)

NIFS-571 A. Iiyoshi, A Komori, A Ejiri, M. Emoto, H Funaba, M Goto, K Ida, H. Idei, S Inagaki, S Kado, O. Kaneko, K. Kawahata, S. Kubo, R. Kumazawa, S Masuzaki, T. Minami, J. Miyazawa, T Morisaki, S Morita, S Murakami, S Muto, T Muto, Y Nagayama,

Y. Nakamura, H. Nakanishi, K. Nanhara, K. Nishimura, N. Noda, T. Kobuchi, S Ohdachi, N. Ohyabu, Y. Oka, M. Osakabe, T. Ozaki, B.J. Peterson, A. Sagara, S. Sakakibara, R. Sakamoto, H. Sasao, M. Sasao, K Sato, M. Sato, T. Seki, T. Shimozuma, M. Shoji, H. Suzuki, Y. Takein, K. Tanaka, K. Toi, T. Tokuzawa, K. Tsumori, I Yamada, H Yamada, S. Yamaguchi, M. Yokoyama, K.Y.Watanabe, T Watari, R. Akiyama, H. Chikaraishi, K. Haba, S. Hamaguchi, S. lima, S Imagawa, N. Inoue, K. Iwamoto, S. Kitagawa, Y. Kubota, J. Kodaira, R. Maekawa, T. Mito. T Nagasaka, A. Nishimura, Y Takita, C. Takahashi, K. Takahata, K. Yamauchi, H. Tamura, T. Tsuzuki, S. Yamada, N. Yanagi, H. Yonezu, Y. Hamada, K. Matsuoka, K. Murai, K. Ohkubo, I. Ohtake, M. Okamoto, S. Sato, T. Satow, S. Sudo, S. Tanahashi, K. Yamazaki, M Fujiwara and O. Motojima,
An Overview of the Large Helical Device Project; Oct. 1998
(IAEA-CN-69/OV1/4)

NIFS-572 M. Fujiwara, H. Yamada, A. Ejiri, M. Emoto, H. Funaba, M. Goto, K. Ida, H. Idei, S. Inagaki, S. Kado, O. Kaneko, K. Kawahata, A. Komori, S. Kubo, R. Kumazawa, S. Masuzaki, T. Minami, J. Miyazawa, T. Morisaki, S. Morita, S. Murakami, S. Muto, T. Muto, Y Nagayama, Y. Nakamura, H. Nakanishi, K. Narihara, K. Nishimura, N. Noda, T. Kobuchi, S. Ohdachi, N. Ohyabu, Y Oka, M. Osakabe, T. Ozaki, B. J. Peterson, A. Sagara, S. Sakakibara, R. Sakamoto, H. Sasao, M. Sasao, K. Sato, M. Sato, T. Seki, T Shimozuma, M. Shoji, H. Sazuki, Y. Takeiri, K. Tanaka, K. Toi, T. Tokuzawa, K. Tsumori, I. Yamada, S. Yamaguchi, M. Yokoyama, K.Y. Watanabe, T. Watari, R. Akiyama, H. Chikaraishi, K. Haba, S. Hamaguchi, M. Iima, S. Imagawa, N. Inoue, K. Iwamoto, S. Kitagawa, Y. Kubota, J. Kodaira, R. Maekawa, T Mito, T. Nagasaka, A. Nishimura, Y. Takita, C Takahashi, K. Takahata, K. Yamauchi, H. Tamura, T. Tsuzuki, S. Yamada, N. Yanagi, H Yonezu, Y Hamada, K. Matsuoka, K. Murai, K. Ohkubo, I. Ohtake, M. Okamoto, S Sato, T. Satow, S Sudo, S. Tanahashi, K. Yamazaki, O. Motojima and A. Iiyoshi,
Plasma Confinement Studies in LHD; Oct. 1998
(IAEA-CN-69/EX2/3)

NIFS-573 O. Motojima, K. Akaishi, H. Chikaraishi, H. Funaba, S. Hamaguchi, S. Imagawa, S. Inagaki, N. Inoue, A. Iwamoto, S. Kitagawa, A. Komori, Y. Kubota, R. Maekawa, S. Masuzaki, T. Mito, J. Miyazawa, T. Morisaki, T. Muroga, T. Nagasaka, Y. Nakmura, A. Nishimura, K. Nishimura, N. Noda, N. Ohyabu, S. Sagara, S. Sakakibara, R. Sakamoto, S. Satoh, T. Satow, M. Shoji, H. Suzuki, K. Takahata, H. Tamura, K. Watanabe, H. Yamada, S. Yamada, S. Yamaguchi, K. Yamazaki, N. Yanagi, T. Baba, H. Hayashi, M. Iima, T. Inoue, S. Kato, T. Kato, T. Kondo, S. Moriuchi, H. Ogawa, I. Ohtake, K. Ooba, H. Sekiguchi, N. Suzuki, S. Takami, Y. Taniguchi, T Tsuzuki, N. Yamamoto, K. Yasui, H. Yonezu, M. Fujiwara and A. Iiyoshi,
Progress Summary of LHD Engineering Design and Construction; Oct 1998
(IAEA-CN-69/FT2/1)

NIFS-574 K Toi, M. Takechi, S. Takagi, G. Matsunaga, M. Isobe, T Kondo, M. Sasao, D.S. Darrow, K. Ohkuni, S. Ohdachi, R. Akiyama A. Fujisawa, M. Gotoh, H. Idei, K. Ida, H. Iguchi, S. Kado, M. Kojima, S. Kubo, S Lee, K. Matsuoka, T. Minami, S. Morita, N. Nikai, S. Nishimura, S. Okamura, M. Osakabe, A. Shimizu, Y. Shirai, C. Takahashi, K. Tanaka, T. Watari and Y. Yoshimura,
Global MHD Modes Excited by Energetic Ions in Heliotron/Torsatron Plasmas, Oct. 1998
(IAEA-CN-69/EXP1/19)

NIFS-575 Y. Hamada, A. Nishizawa, Y. Kawasumi, A. Fujisawa, M. Kojima, K. Narihara, K. Ida, A. Ejiri, S. Ohdachi, K. Kawahata, K. Toi, K. Sato, T. Seki, H. Iguchi, K. Adachi, S. Hidekuma, S.Hirokura, K. Iwasaki, T. Ido, R. Kumazawa, H. Kuramoto, T. Minami, I.. Nomura, M. Sasao, K.N. Sato, T. Tsuzuki, I. Yamada and T. Watari,
Potential Turbulence in Tokamak Plasmas; Oct. 1998
(IAEA-CN-69/EXP2/14)

NIFS-576 S. Murakami, U. Gasparino, H. Idei, S. Kubo, H. Maassberg, N. Marushchenko, N. Nakajima, M. Romé and M. Okamoto,
5D Simulation Study of Suprathermal Electron Transport in Non-Axisymmetric Plasmas; Oct. 1998
(IAEA-CN-69/THP1/01)

NIFS-577 S. Fujiwara and T. Sato,
Molecular Dynamics Simulation of Structure Formation of Short Chain Molecules; Nov. 1998

NIFS-578 T. Yamagishi,
Eigenfunctions for Vlasov Equation in Multi-species Plasmas Nov 1998

NIFS-579 M. Tanaka, A. Yu Grosberg and T Tanaka,
Molecular Dynamics of Strongly-Coupled Multichain Coulomb Polymers in Pure and Salt Aqueous Solutions; Nov. 1998

NIFS-580 J. Chen, N. Nakajima and M. Okamoto,
Global Mode Analysis of Ideal MHD Modes in a Heliotron/Torsatron System: I. Mercier-unstable Equilibria; Dec. 1998

NIFS-581 M. Tanaka, A. Yu Grosberg and T. Tanaka,
Comparison of Multichain Coulomb Polymers in Isolated and Periodic Systems: Molecular Dynamics Study; Jan. 1999

NIFS-582 V.S. Chan and S. Murakami,
Self-Consistent Electric Field Effect on Electron Transport of ECH Plasmas; Feb. 1999

NIFS-583 M. Yokoyama, N. Nakajima, M. Okamoto, Y. Nakamura and M. Wakatani,
Roles of Bumpy Field on Collisionless Particle Confinement in Helical-Axis Heliotrons; Feb. 1999